Nano Research

Open Access

Research Article

Dynamic conformational changes in the molecular rotor of the triangular-shaped AIEgens linker enable diversification of Ln-MOFs with a family of three-connected networks

De-Xin Chen[1,§], Yun-Lan Li[3,§], Ru-Yan Li[1], Wen-Wen Qin[2], Hai-Ling Wang[1] ✉, Hua-Hong Zou[2] ✉, Fu-Pei Liang[2] ✉, and Zhong-Hong Zhu[1] ✉

[1] *School of Chemistry and Chemical Engineering, Guangxi Key Laboratory of Electrochemical Energy Materials, Guangxi University, Nanning 530004, China*
[2] *Key Laboratory for Chemistry and Molecular Engineering of Medicinal Resources (Ministry of Education of China), Guangxi Key Laboratory of Chemistry and Molecular Engineering of Medicinal Resources, School of Chemistry and Pharmaceutical Sciences, Guangxi Normal University, Guilin 541004, China*
[3] *School of Resources, Environment and Materials, Guangxi University, Nanning 530004, China*
§ *De-Xin Chen and Yun-Lan Li contributed equally to this work.*

Cite this article: *Nano Research*, **2026**, *19*, 94908442. https://doi.org/10.26599/NR.2026.94908442

ABSTRACT: Regulating reaction conditions to manipulate the twisting angle or conformational changes of the molecular rotor modules in triangular-shaped aggregation-induced emission luminogens (AIEgens) can induce the formation of lanthanide metal-organic frameworks (Ln-MOFs) with 3,8-c, 3^2,8-c, and 3^3,11-c connected network structures, significantly enriching the 3-c connected network family. This work, to our knowledge, is the first to reveal that alterations in the twist angles of molecular rotor modules in triangular-shaped AIEgens can lead to a serial expansion of the family of topological networks based on 3-c connections. Surprisingly, both Eu-MOF and Tb-MOF display linear temperature responses with varying sensitivities in the high and low temperature regions, respectively, facilitating the construction of a dual-region ratiometric fluorescence thermometer. What is more noteworthy is that Tb-MOF can be easily and efficiently fabricated into thin films, maintaining stable and bright yellow-green luminescence even after multiple foldings, which demonstrates its excellent mechanical flexibility and processability potential. This study not only charts a new course for expanding the topological network structure of Ln-MOFs through dynamic AIEgens but also broadens the horizons for the optical applications of multifunctional Ln-MOFs emitters.

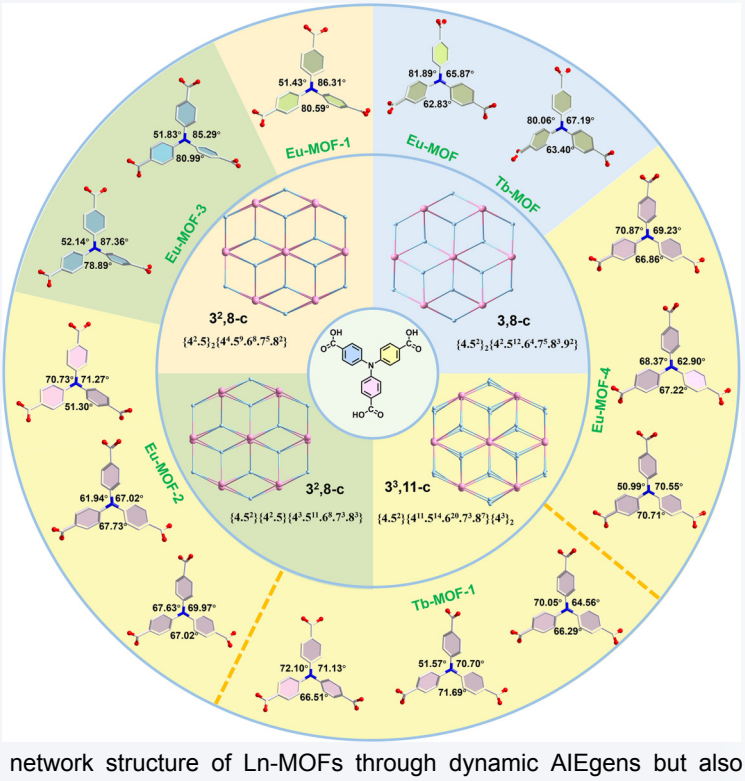

KEYWORDS: lanthanide metal-organic frameworks, aggregation-induced emission luminogens, three-connected networks, topological connections, lanthanide luminescence

Received: December 5, 2025; **Revised:** January 10, 2026; **Accepted:** January 13, 2026

✉Address correspondence to Hai-Ling Wang, whling@gxu.edu.cn; Hua-Hong Zou, gxnuchem@foxmail.com; Fu-Pei Liang, liangfupei@glut.edu.cn; Zhong-Hong Zhu, zzhong@gxu.edu.cn

1 Introduction

Metal-organic frameworks (MOFs), a class of long-range ordered and highly customizable crystalline porous materials, are formed by alternating connections between secondary building units (SBUs) and linkers through coordination interactions [1–5]. Currently, customizing the structure of MOFs mainly depends on the following two aspects: regulating the type, length, and functional group of the linker, and systematically regulating the geometric configuration and connection method of SBUs [6–8]. However, the structural design of traditional MOFs is often limited to the use of linear or planar rigid organic linkers, which significantly restricts the expansion of diversified topological connection networks. After selecting these rigid linkers, the network structure of MOFs is mainly expanded by the diverse connection modes of SBUs [9, 10]. In 2001, Tang et al. discovered that organic molecules containing molecular rotor modules exhibited obvious aggregation-induced emission (AIE) behavior, and these AIE luminogens (AIEgens) have obviously received widespread attention [11–13]. More importantly, AIEgens often possess dynamic molecular rotor modules, exhibiting non-planar and twisted molecular conformations. Obviously, using AIEgens as functionalized linkers and introducing them into the structure of MOFs can effectively break through the geometric constraints of traditional rigid "static" linkers [14, 15]. In 2025, our team assembled a smart luminescent MOF (Zr-TPE-MOF) using tetraphenylethylene-based AIEgen (4′,4″,4‴,4⁗-(ethene-1,1,2,2-tetrayl)tetrabiphenyl-4-carboxylic acid (H_4TPPE)) with an extended molecular rotor structure as a linker, and octahedral $Zr_6O_4(OH)_8(H_2O)_4$ clusters as SBUs. This MOF exhibits a breathing behavior driven by CH_2Cl_2 or CH_3COOH vapor. The entry of trace amounts of CH_2Cl_2 or CH_3COOH vapor into the pores triggers changes in the motion and torsion of the molecular rotors within the Zr-TPE-MOF structure, leading to a significant blue shift in the ligand emission wavelength and an increase in emission intensity [16]. In 2021, Tang et al. synthesized several dynamic MOFs (Zn/CoMOFs, ZnTCPE, and ZnETTB) using tetraphenylethylene carboxylic acid derivative ligands. They demonstrated that perturbations from specific guest molecules, temperature, or pressure could effectively induce changes in the movement or twisting degree of the molecular rotor ligands within the pores, leading to noticeable fluorescence color changes [17, 18]. During the process of coordination self-assembly to form specific MOFs, the dynamic behavior and conformational flexibility of AIEgens enable them to respond to changes in external conditions such as solvent polarity, temperature, pressure, and acidity and alkalinity, and dynamically adjust their spatial orientation and coordination mode, thereby significantly broadening the diversified topological connection network of MOFs [19–23]. The dynamic adaptive behavior of AIEgens not only helps to guide the formation of rare topological networks of MOFs that are difficult to construct with traditional rigid linkers, but also can systematically expand the diversified topological connection networks of MOFs [24]. Farha et al. regulated the dihedral angle of V-shaped dicarboxylic acid ligands by replacing the C–H groups of the aromatic ring with nitrogen atoms, obtaining three different topological types of Zr-MOFs. This demonstrated that altering the dihedral angle of the rotor module can effectively promote the structural design process of MOFs [25]. However, it is still rare to exploit the twisting and conformational changes of molecular rotor modules in AIEgens to serially expand dynamic topologically connected networks of MOFs. Clearly, the exploration of manipulating twisted and dynamic AIEgens as linkers to customize the synthesis of MOFs is significantly insufficient. Further in-depth analysis of the controllable assembly of AIEgens containing dynamic modules to form MOFs and their topological evolution will help expand the development of diversified topological connection networks.

Using AIEgens as linkers not only expands the topological connection network of diversified MOFs, but also breaks through the huge bottleneck of traditional organic fluorophores that are prone to fluorescence quenching in the aggregated state [26–29]. The AIEgens core, represented by triphenylamine (TPA), has attracted widespread attention due to its propeller-shaped configuration and excellent photophysical properties [30, 31]. In 2022, Bu et al. reported a Zn-MOF (NKU-128) assembled from an AIEgen based on a triphenylamine core (tri(4-(pyridine-3-yl)phenyl)amine (3-TPPA)) and Zn(II) ions. They utilized temperature, pressure, and solvent-induced dynamic changes in the motion and distortion of the molecular rotor structure of the ligand to achieve full-spectrum fluorescence tuning [32]. In 2025, our team utilized triphenylamine carboxylic acid derivative ligands (4,4′,4″-triphenylamine tricarboxylate (TPA-COOH)) to construct intelligent lanthanide-based luminescent MOFs with adaptive antenna effects. We precisely controlled the energy transfer pathways, achieving highly efficient intelligent luminescence switching behavior and multiple intelligent anti-counterfeiting applications [33]. Obviously, the optical behaviors and energy levels of AIEgens with dynamic modules are closely related to their molecular configurations and the motion of the rotors. Micro-perturbations of AIEgens by the external environment can easily cause the molecular rotors to exhibit rapid changes in the degree of motion or twisting, thereby inducing dynamic changes in their energy levels [14, 15, 20, 28, 34, 35]. Lanthanide ions or lanthanide clusters with outstanding photophysical properties and fingerprint emission spectra are used as SBUs and alternately connected with dynamic molecular rotors as linkers to self-assemble into dynamic lanthanide MOFs (Ln-MOFs), which opens up new horizons for constructing new artificial intelligence luminescent materials [28, 35]. The changes in energy levels caused by the degree of distortion and conformational changes of the molecular rotors of the AIEgens ligands can achieve an adaptive "antenna effect" for lanthanide ions at different energy levels, thereby effectively constructing artificial intelligence multicolor/color-changing materials [33]. Therefore, combining the dynamic responsiveness of AIEgens with the fingerprint emission characteristics of lanthanide ions can effectively overcome the shortcomings of traditional Ln-MOFs, such as single structure, low intelligent response sensitivity, and delayed response, and open up a new blueprint for the development of new intelligent luminescent materials.

Herein, the classic AIEgen TPA-COOH and $Ln(NO_3)_3{\cdot}6H_2O$ (Ln = Eu and Tb) were used to successfully obtain two Ln-MOFs (Eu-MOF and Tb-MOF) with the same topological network through "one-pot" solvothermal reaction (Scheme 1 and Table S1 in the Electronic Sullementary Material (ESM)). Although Eu-MOF and Tb-MOF are highly similar in overall structure and both exhibit 3,8-c topological connection mode and topological lattice ($\{4.5^2\}_2\{4^2.5^{12}.6^4.7^5.8^3.9^2\}$), there are slight variations in the angles of the benzene rings in the AIEgens within the two structures. By adjusting the reaction conditions to influence the twisting angle and conformational changes of the molecular rotor module, Eu/Tb-MOF-1 and Eu-MOF-2-4 were obtained, respectively. Among these, Eu-MOF-1 and Eu-MOF-3 form complex 3^2,8-c connection

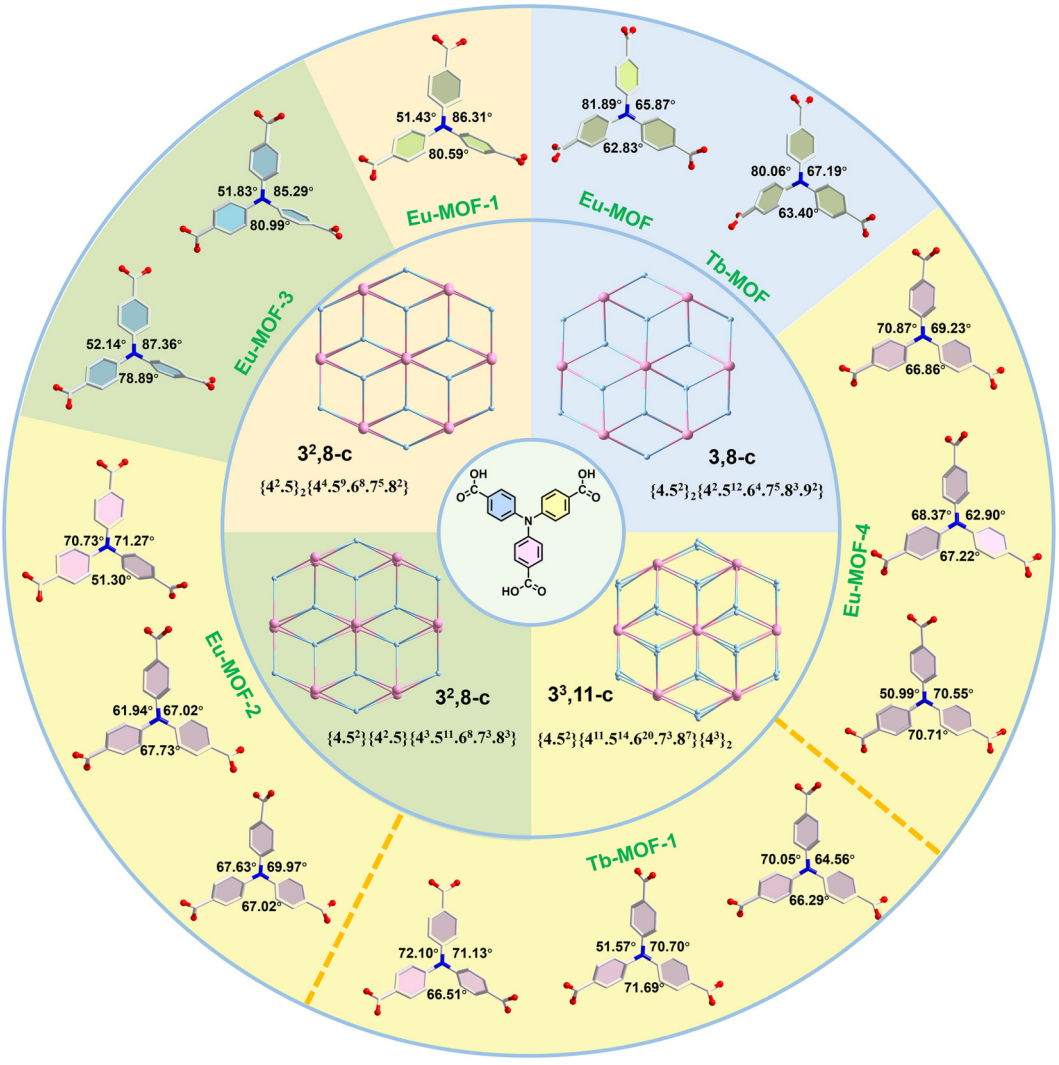

Scheme 1 Schematic diagram of the topological network of Ln-MOFs with 3-c connections, which was extended by the classic AIEgens TPA-COOH.

networks, with topological point symbols of $\{4^2.5\}_2\{4^4.5^9.6^8.7^5.8^2\}$ and $\{4.5^2\}\{4^2.5\}\{4^3.5^{11}.6^8.7^3.8^3\}$ (Table S1 in the ESM), respectively. Eu-MOF-2/4 and Tb-MOF-1 developed a more intricate 3^3,11-c connection network, with topological point symbols of $\{4.5^2\}\{4^{11}.5^{14}.6^{20}.7^3.8^7\}\{4^3\}_2$ (Scheme 1 and Table S1 in the ESM). As far as we know, this work is the first to demonstrate that regulating the twisting angle and conformational changes of the molecular rotor module within AIEgens can achieve a serial expansion of the Ln-MOFs family with 3-c connected networks. AIEgens with varying torsion angles possess distinct energy levels, allowing them to meet the excitation wavelength requirements of specific lanthanide ions. Consequently, Tb-MOF and Eu-MOF exhibit different optimal excitation wavelengths. Specifically, 365 nm excitation light aligns better with the energy level of Tb^{3+} ions, while 410 nm excitation is more effective for exciting Eu^{3+} ions, enabling selective luminescence control based on the excitation wavelength. Additionally, Eu-/Tb-MOF displays linear temperature responses with different slopes in high/low temperature regions, making it suitable for constructing a dual-segment ratiometric fluorescence temperature sensing system. It is worth noting that Tb-MOF can be easily and quickly fabricated into thin film material, maintaining stable and bright green luminescence even after multiple bends, indicating good processing performance and potential for device applications. This study achieved the systematic construction of Ln-MOFs with diverse topological connection networks by regulating reaction conditions to manipulate the twisting angle or conformational changes of the molecular rotor modules. This work not only marks significant progress in the crystal engineering of dynamic Ln-MOFs but also opens new avenues for the systematic development of multifunctional Ln-MOFs emitters.

2 Results and discussion

2.1 Structural analysis

The classic molecular rotor ligand TPA-COOH was reacted with $Ln(NO_3)_3{\cdot}6H_2O$ (Ln = Eu and Tb) in a "one-pot" solvothermal reaction, successfully yielding yellow-brown bulk crystals (Eu-MOF) and gray-green bulk crystals (Tb-MOF) (Fig. 1(a)). Single crystal X-ray diffraction (SCXRD) analysis revealed that both Eu-MOF and Tb-MOF crystallized in the monoclinic $P2_1/n$ space group (Table S2 in the ESM). Eu-MOF features a three-dimensional layered structure with a fishnet-like structure formed by staggered and antiparallel TPA-COO^- linkers connecting EuO_8 polyhedrons (Fig. 1(b) and Fig. S1(a) in the ESM). The SBU within the Eu-MOF structure consists of two EuO_8 polyhedra linked by

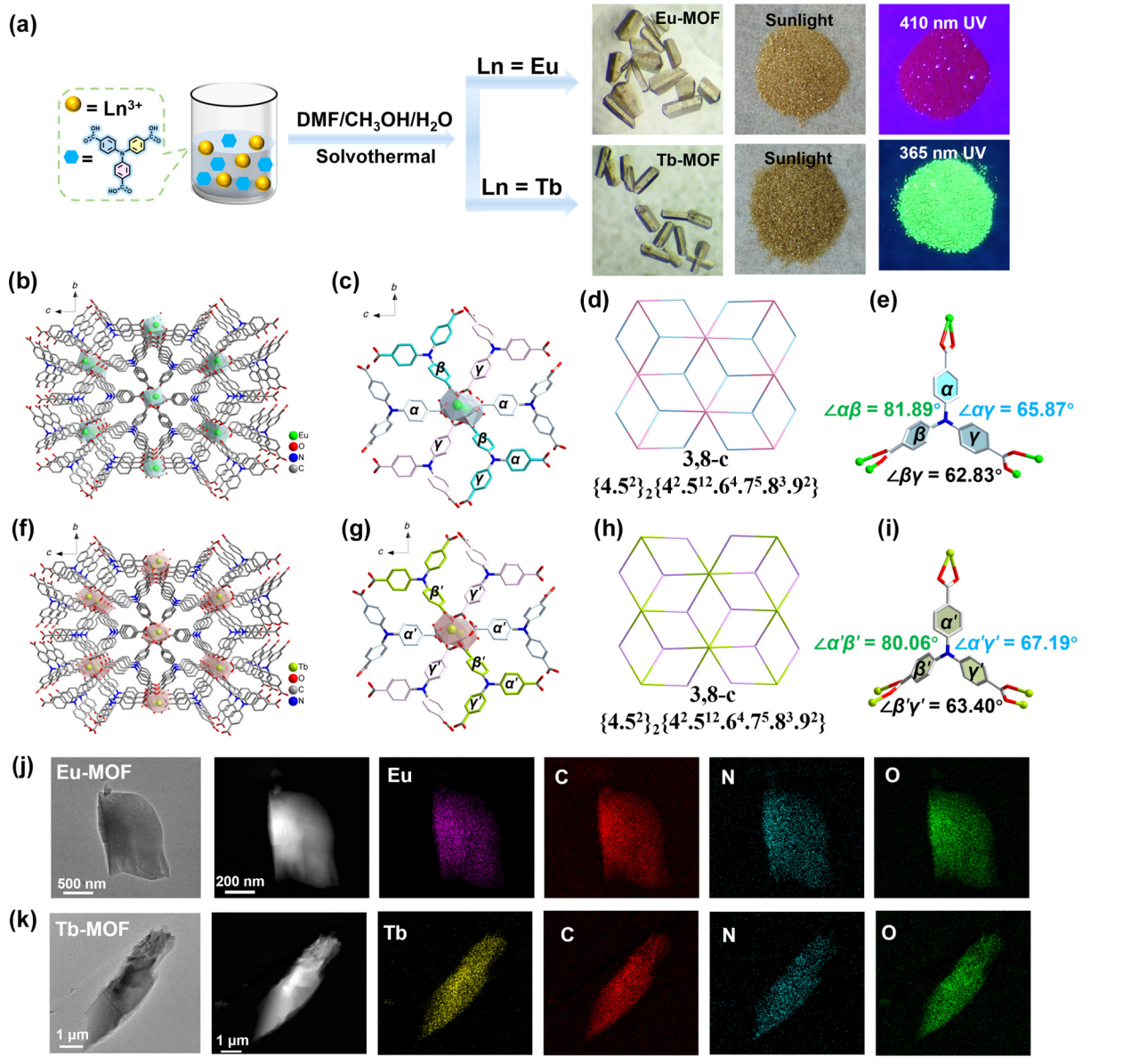

Figure 1 (a) Schematic diagram of the synthesis of Ln-MOFs from Ln^{3+} and TPA-COOH. ((b) and (f)) Crystal structures of Eu-MOF and Tb-MOF. ((c) and (g)) In the *a*-direction, TPA-COO^- linkers connect the three SBUs of Eu-MOF and Tb-MOF. ((d) and (h)) Topological connection modes of Eu-MOF and Tb-MOF. ((e) and (i)) Angle between benzene rings and ligand coordination mode on TPA-COO^-. ((j) and (k)) TEM images and EDS elemental mapping of Eu-MOF and Tb-MOF.

eight twisted TPA-COO^- linkers (Figs. S1(b) and S1(c) in the ESM). In addition, the α, β, and γ planes of the phenyl rings of the TPA-COO^- linkers attached to the same SBU are arranged in a clockwise direction (Fig. 1(c)). Each Eu^{3+} ion in the SBU is connected to five molecular rotor ligands and two terminally coordinated H_2O molecules (Fig. S1(d) in the ESM). Topological analysis indicates that the connection mode of Eu-MOF is 3,8-c, with a topological point symbol of $\{4.5^2\}_2\{4^2.5^{12}.6^4.7^5.8^3.9^2\}$ (Fig. 1(d)). The angles between the three benzene rings of the twisted molecular rotor linker are 81.89°, 65.87°, and 62.83°, respectively (Fig. 1(e)). The structures of Tb-MOF and Eu-MOF are highly similar (Fig. 1(f) and Figs. S1(e)–S1(h) in the ESM), both exhibiting a 3,8-c topological connection mode and a topological point connection of $\{4.5^2\}_2\{4^2.5^{12}.6^4.7^5.8^3.9^2\}$ (Fig. 1(h)), though there are subtle differences in the degree of distortion of the dynamic molecular rotor in the structure. The angles between the three benzene rings of the dynamic molecular rotor in the Tb-MOF structure are 80.06°, 67.19°, and 63.40°, respectively (Fig. 1(i)). The α, β, and γ planes of the linker benzene ring connected to SBU are also arranged in the clockwise direction (Fig. 1(g)). The TPA-COO^- linker in both structures has only one coordination mode: μ_5-η^2:η^1:η^1:η^1:η^1 (Figs. 1(e) and 1(i)).

Eu-MOF and Tb-MOF exhibit similar Fourier transform infrared characteristic absorption peaks, with distinct peaks near 3420, 1600, 1400, and 1320 cm^{-1}, corresponding to ν(O–H), ν(C=C), ν(C–N), and ν(C–O) characteristic vibration absorption peaks, respectively, consistent with the functional groups in the structure (Fig. S7 in the ESM) [36, 37]. Thermogravimetric analysis results indicate that the guest molecules in both MOFs are DMF, CH_3OH, and water molecules (Fig. S8 in the ESM). The experimental values of powder X-ray diffraction (PXRD) closely matched the simulated values, confirming that the obtained Eu-

MOF and Tb-MOF were pure phases (Fig. S9 in the ESM). Scanning electron microscopy (SEM) and high-resolution transmission electron microscopy (HR-TEM) images show that both MOFs are regular and distinct bulk crystals with very clean surfaces (Fig. S10 in the ESM). Energy dispersive X-ray spectroscopy (EDS) measurements performed in HR-TEM mode show that Eu/Tb, C, N, and O elements are uniformly distributed (Figs. 1(j) and 1(k)).

To advance the crystal engineering of dynamic MOFs, we successfully synthesized two crystals with distinct topological connections by adding camphoric acid (Cam), adjusting the metal-to-ligand molar ratio, optimizing the solvent composition, and extending the stirring time: This resulted in rhombus-shaped orange crystals of Eu-MOF-1 and needle-shaped yellow crystals of Eu-MOF-2 (Fig. 2(a)). SCXRD analysis revealed that Eu-MOF-1 and Eu-MOF-2 crystallized in monoclinic $C2/c$ and $P2_1/c$ space groups, respectively (Table S2 in the ESM). The structure of Eu-MOF-1 is characterized by TPA-COO^- linkers interlacedly connecting EuO_9 polyhedra (Fig. 2(b) and Fig. S2(a) in the ESM). The SBU within the Eu-MOF-1 structure consists of two EuO_9 polyhedra linked by eight twisted TPA-COO^- linkers (Figs. S2(b) and S2(c) in the ESM). Each Eu^{3+} ion in the SBU is connected to five molecular rotor ligands, a bridging oxygen atom, and a terminally coordinated H_2O molecule (Fig. S2(d) in the ESM). Two SBUs are linked by a TPA-COO^- linker to form a staggered overlapping bilayer structure (Fig. 2(c) and Fig. S2(b) in the ESM). Topological analysis indicates that the connection mode of Eu-MOF-1 is 3^2,8-c, with a topological point symbol of $\{4^2.5\}_2\{4^4.5^9.6^8.7^5.8^2\}$ (Fig. 2(d)). The angles between the three benzene rings of the twisted molecular rotor ligand are 51.43°, 80.59°, and 86.31°, respectively (Fig. 2(h)). Notably, although there is only one degree of twisting molecular rotor in the Eu-MOF and Eu-MOF-1 structures, the dynamic molecular rotor in the Eu-MOF-1 structure is significantly twisted due to the regulation of reaction conditions. This affects its spatial lattice arrangement, and induces the formation of dynamic MOFs structures with different topological connections, offering a novel method for expanding the topological structure of 3,8-c. The SBU of Eu-MOF-2 consists of 11 TPA-COO^- linkers connecting one EuO_8 polyhedron and two EuO_9 polyhedra, and the two SBUs linked by the linkers form a staggered and overlapping three-layer structure (Figs. 2(e) and 2(f), and Figs. S3(a)–S3(d) in the ESM). In each SBU, Eu_1 and Eu_2 are connected to six molecular rotor ligands, while Eu_3 is connected to five (Figs. S3(e)–S3(g) in the ESM). The angles between the TPA-COO^- linker benzene rings in Eu-MOF-2 are divided into three groups, which are 70.73°, 51.30°, and 71.27°; 61.94°, 67.73°, and 67.02°; and 67.63°, 67.02°, and 69.97° (Fig. 2(i)). Topological analysis shows that the connection mode of Eu-MOF-2 is 3^3,11-c, with topological point symbols of $\{4.5^2\}\{4^{11}.5^{14}.6^{20}.7^3.8^7\}\{4^3\}_2$ (Fig. 2(g)). The TPA-COO^- linker in the Eu-MOF-1 structure has a single coordination mode: μ_5-η^2:η^1:η^1:η^1:η^1 (Fig. 2(h)). In contrast, the linkers in Eu-MOF-2 exhibit two different coordination modes: μ_5-η^2:η^1:η^1:η^1:η^1 and μ_6-η^1:η^1:η^1:η^1:η^1:η^1 (Fig. 2(i)). HR-TEM shows that both Eu-MOF-1 and Eu-MOF-2 are blocky crystals with clean surfaces, and the elements are uniformly distributed (Figs. 2(j) and 2(k)).

When $Tb(NO_3)_3{\cdot}6H_2O$ replaced $Eu(NO_3)_3{\cdot}6H_2O$, only one bulk crystal (Tb-MOF-1) was obtained (Fig. 3(a)). The structure of Tb-MOF-1 is similar to that of Eu-MOF-2 (Figs. 3(b)–3(d), and Figs. S4(a) and S4(c)–S4(f) in the ESM), but the SBU of Tb-MOF-1 consists of one TbO_7 and two TbO_9 polyhedra (Fig. S4(b) in the ESM). The angles between the TPA-COO^- linker benzene rings are 72.10°, 66.51°, and 71.13°; 70.05°, 66.29°, and 64.56°; and 51.57°, 71.69°, and 70.70°. Its coordination mode is μ_6-η^1:η^1:η^1:η^1:η^1:η^1 and μ_5-η^2:η^1:η^2:η^1:η^1 (Fig. 3(e)). HR-TEM proves that Tb-MOF-1 is a block crystal with a clean surface and a uniform element distribution (3(f)). Overall, adjusting the reaction conditions can significantly affect the distortion degree of the dynamic molecular rotor, thereby altering the SBU composition and the coordination mode of the dynamic molecular rotor. This ultimately leads to the formation of topologies with varied spatial lattice arrangements, significantly enriching the diversity of the (3-c) topological family.

One factor that regulates the reaction process is the stirring time. By simply extending the stirring time to 4.5 h, two crystals with distinct new topological connections were unexpectedly obtained: the orange block-like Eu-MOF-3 and gray-green flake-like Eu-MOF-4 (Fig. 4(a)). SCXRD analysis revealed that both Eu-MOF-3 and Eu-MOF-4 crystallized in the monoclinic $P2_1/c$ space group (Table S2 in the ESM). Eu-MOF-3 is composed of TPA-COO^- linkers that alternately connect EuO_9 polyhedra, forming a diamond-shaped three-dimensional layered structure (Fig 4(b) and Fig. S5(a) in the ESM). The SBU within the Eu-MOF-3 structure is composed of two EuO_9 polyhedra, with Eu^{3+} ions in the SBU connected to five TPA-COO^- linkers, a terminal-coordinated H_2O molecule, and a bridging oxygen atom (Figs. S5(b)–S5(d) in the ESM). Two SBUs are linked by TPA-COO^- linkers to create a staggered overlapping bilayer structure (Fig. 4(c), and Figs. S5(e) and S5(f) in the ESM). In the Eu-MOF-3 structure, the twisted molecular rotor ligands have two groups of angles between the three benzene rings: 51.83°, 80.99°, and 85.29°; and 52.14°, 78.89°, and 87.36°, respectively. The TPA-COO^- linkers exhibit only one coordination mode: μ_5-η^2:η^1:η^1:η^1:η^1 (Fig. 4(h)). Topological analysis indicates that the connection mode of Eu-MOF-3 is 3^2,8-c, with topological point symbols of $\{4.5^2\}\{4^2.5\}\{4^3.5^{11}.6^8.7^3.8^3\}$ (Fig. 4(d)). It is worth noting that the prolonged reaction stirring time caused significant distortion of the dynamic molecular rotor in the Eu-MOF-3 structure, which in turn triggered the rearrangement of the spatial lattice within the crystal, ultimately altering its overall topological network. The structural features of Eu-MOF-4 closely resemble those of Eu-MOF-2 and Tb-MOF-1 (Figs. 4(e)–4(g) and Figs. S6(a)–S6(f) in the ESM); their topological connection patterns and topological point symbols are 3^3,11-c and $\{4.5^2\}\{4^{11}.5^{14}.6^{20}.7^3.8^7\}\{4^3\}_2$, with the only difference being the varying dihedral angles of the benzene ring in the TPA-COO^- linkers. The angles between the linker benzene rings in Eu-MOF-4 fall into three groups: 50.99°, 70.55°, and 70.71°; 70.87°, 66.86°, and 69.23°; and 68.37°, 67.22°, and 62.90° (Fig. 4(i)). These findings demonstrate that prolonging the reaction stirring time can significantly enhance the twisting of the dynamic molecular rotor, thereby altering the SBU composition and the coordination mode of the dynamic molecular rotor, ultimately inducing the formation of two distinct 3-c connection topological networks, achieving diversified regulation of the topological structure.

By precisely controlling the aforementioned series of structures, it was successfully demonstrated that the twisting angle control based on the dynamic molecular rotor ligand can effectively guide the selection of different coordination assembly paths with the lanthanide ion SBU, thereby constructing a framework material with a novel topological structure. This strategy significantly expands the MOF structural family based on 3-c topology,

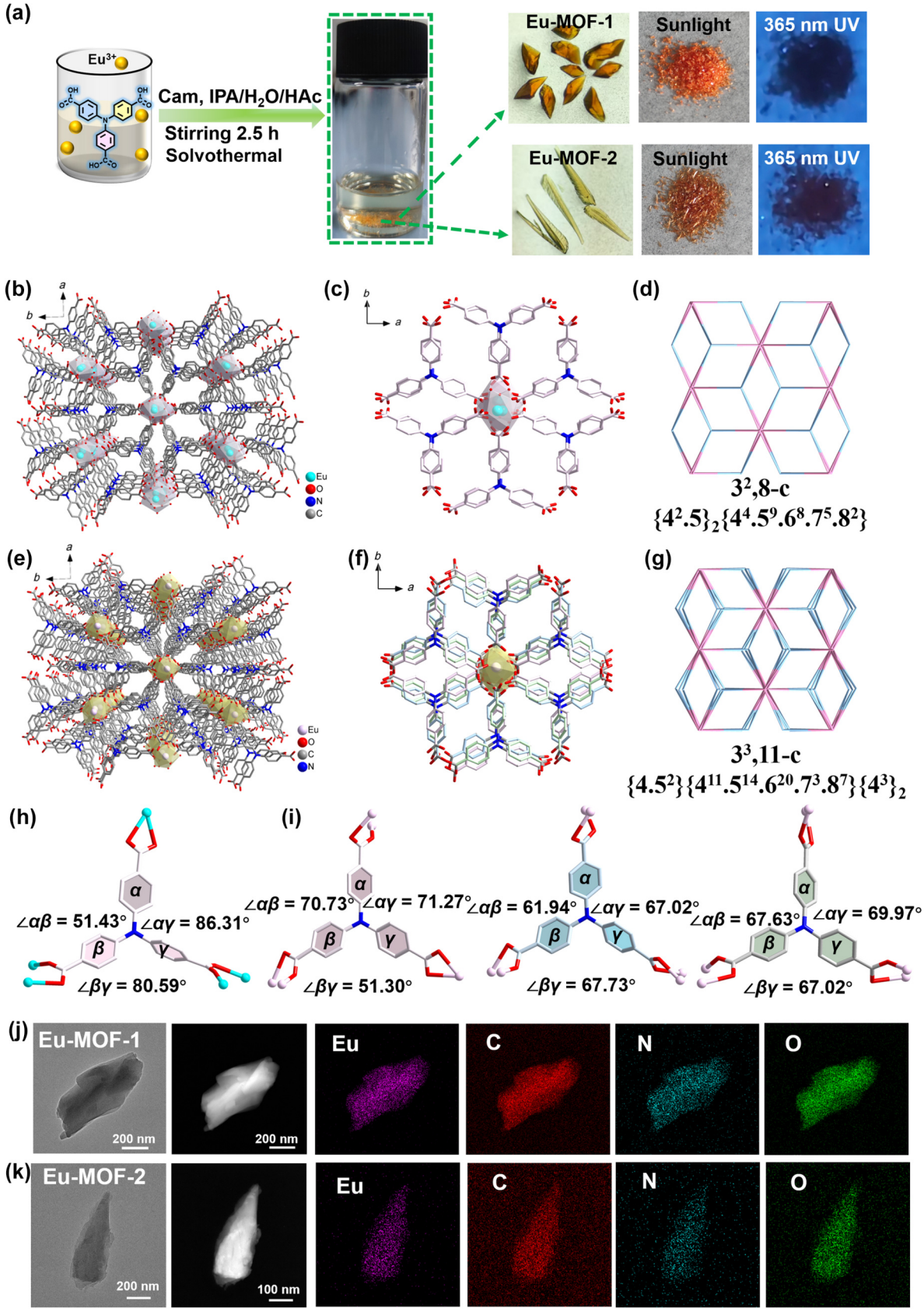

Figure 2 (a) Schematic diagram of the synthesis of Eu-MOF-1/2 from Eu^{3+} and TPA-COOH. ((b) and (e)) Crystal structures of Eu-MOF-1 and Eu-MOF-2. ((c) and (f)) In the *c*-direction, $TPA\text{-}COO^-$ linkers connect the two SBUs of Eu-MOF-1 and Eu-MOF-2. ((d) and (g)) Topological connection modes of Eu-MOF-1 and Eu-MOF-2. ((h) and (i)) Angle between benzene rings and ligand coordination mode on $TPA\text{-}COO^-$. ((j) and (k)) TEM images and EDS elemental mapping of Eu-MOF-1 and Eu-MOF-2.

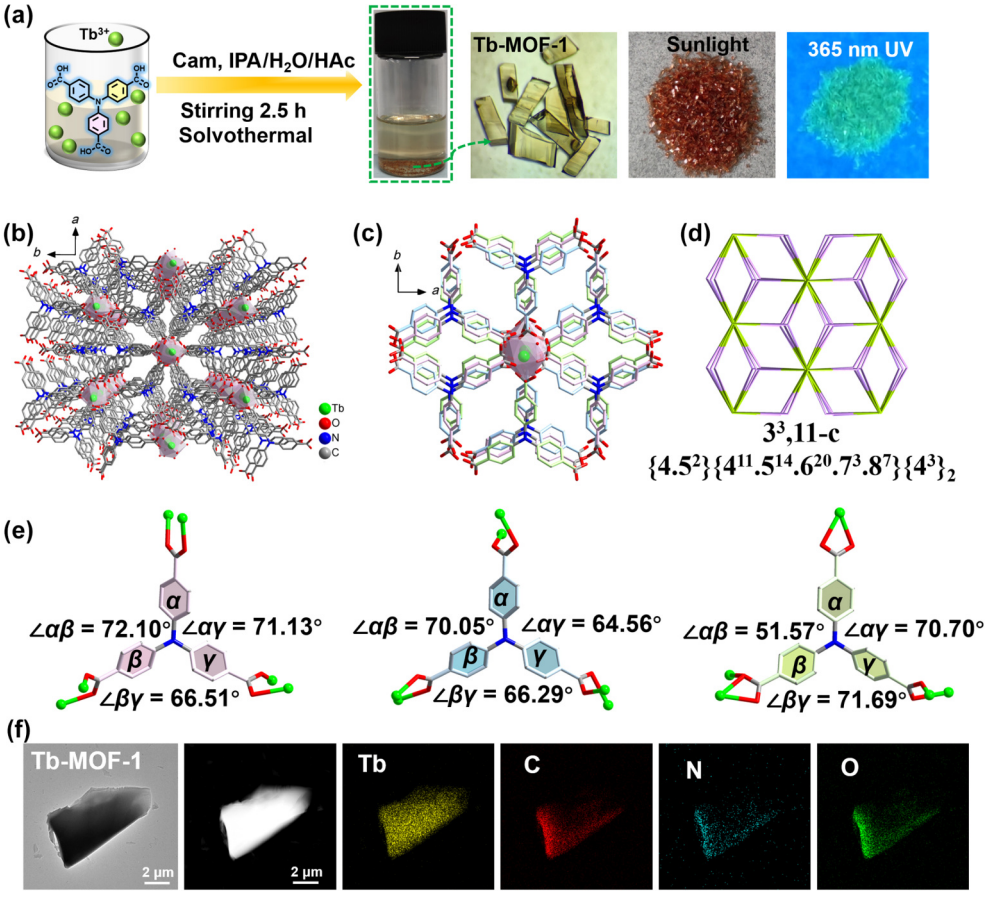

Figure 3 (a) Schematic diagram of the synthesis of Tb-MOF-1 from Tb^{3+} and TPA-COOH. (b) Crystal structure of Tb-MOF-1. (c) In the *c*-direction, $TPA\text{-}COO^-$ linkers connect the two SBUs of Tb-MOF-1. (d) Topological connection mode of Tb-MOF-1. (e) Angle between benzene rings and ligand coordination mode on $TPA\text{-}COO^-$. (f) TEM image and EDS elemental mapping of Tb-MOF-1.

overcoming the limitations of the original type and greatly enriching the diversity and complexity of this topological network. Thus, introducing dynamic molecular rotors into framework materials can not only imparts dynamic response properties (such as structural tunability and adaptive behavior to external stimuli) but also provides a new method for constructing novel topological structures by regulating reaction conditions to induce the twisting changes in dynamic molecular rotors, thereby enriching the crystal engineering of MOFs. Additionally, this type of MOF material with a novel topological structure shows broad application prospects in cutting-edge fields such as high-sensitivity dynamic optical sensing, adaptive photonic devices, and intelligent response systems.

2.2 Photophysical properties

To date, most luminescent MOFs have typically employed planar, rigid, static structures as linkers [38, 39]. The use of triphenylamine-based molecular rotor linkers, which exhibit pronounced AIE properties, offers new opportunities for constructing novel dynamic luminescent MOFs. Conformational changes in the dynamic molecular rotor ligands determine their multiple excitation spectral properties in different Ln-MOFs. We performed ultraviolet–visible (UV–Vis) absorption spectroscopy tests on Eu-MOF and Tb-MOF, respectively. Both showed distinct absorption peaks at 315 and 385 nm, attributed to the $\pi \rightarrow \pi^*$ and $n \rightarrow \pi^*$ electronic transitions in the TPA-COOH ligand, respectively (Fig. S11(a) in the ESM) [30, 33, 40]. Based on the excitation spectra of Eu-MOF and Tb-MOF (Figs. S11(b) and S11(c) in th ESM), it is reasonable to choose 410 and 365 nm as the optimal excitation wavelengths for Eu-MOF and Tb-MOF, respectively. As shown in Fig. 5(a), Tb-MOF exhibits emission peaks at 488, 543, 584, and 619 nm, which can be assigned to the $^5D_4 \rightarrow {}^7F_{6-3}$ energy level transitions of Tb^{3+} ions, respectively. Eu-MOF exhibits characteristic emissions of Eu^{3+} ions at 590, 614, 649, and 694 nm, respectively, which can be assigned to the $^5D_0 \rightarrow {}^7F_{1-4}$ energy level transitions (Fig. 5(b)). The excitation–emission-dependent three-dimensional spectra of Eu-MOF and Tb-MOF reveal distinct emission centers within the excitation ranges of 380–460 and 350–420 nm, respectively. Furthermore, none of these emission peaks exhibits clear excitation-dependent behavior but rather has an optimal excitation wavelength range (Figs. 5(c) and 5(d)). The luminescence quantum yields of Eu-MOF and Tb-MOF are 1.58% and 2.12%, respectively; the luminescence lifetimes are 236.37 and 260.34 μs, respectively (Figs. S12(a)–S12(d) in the ESM). In the Eu-MOF-1/2/3/4 series of structures, the benzene rings between the $TPA\text{-}COO^-$ ligands are closely packed, leading to strong π–π interactions. This π–π stacking facilitates the return of excited state energy to the ground state through non-radiative transitions, preventing efficient energy transfer to the luminescent center and thus suppressing radiative emission (Fig. S11(d) in the ESM).

Literature research revealed that derivatives with triphenylamine as the core structural unit demonstrate significant and tunable afterglow luminescence behavior in terms of photophysical properties [41–44]. Based on the excellent photophysical properties

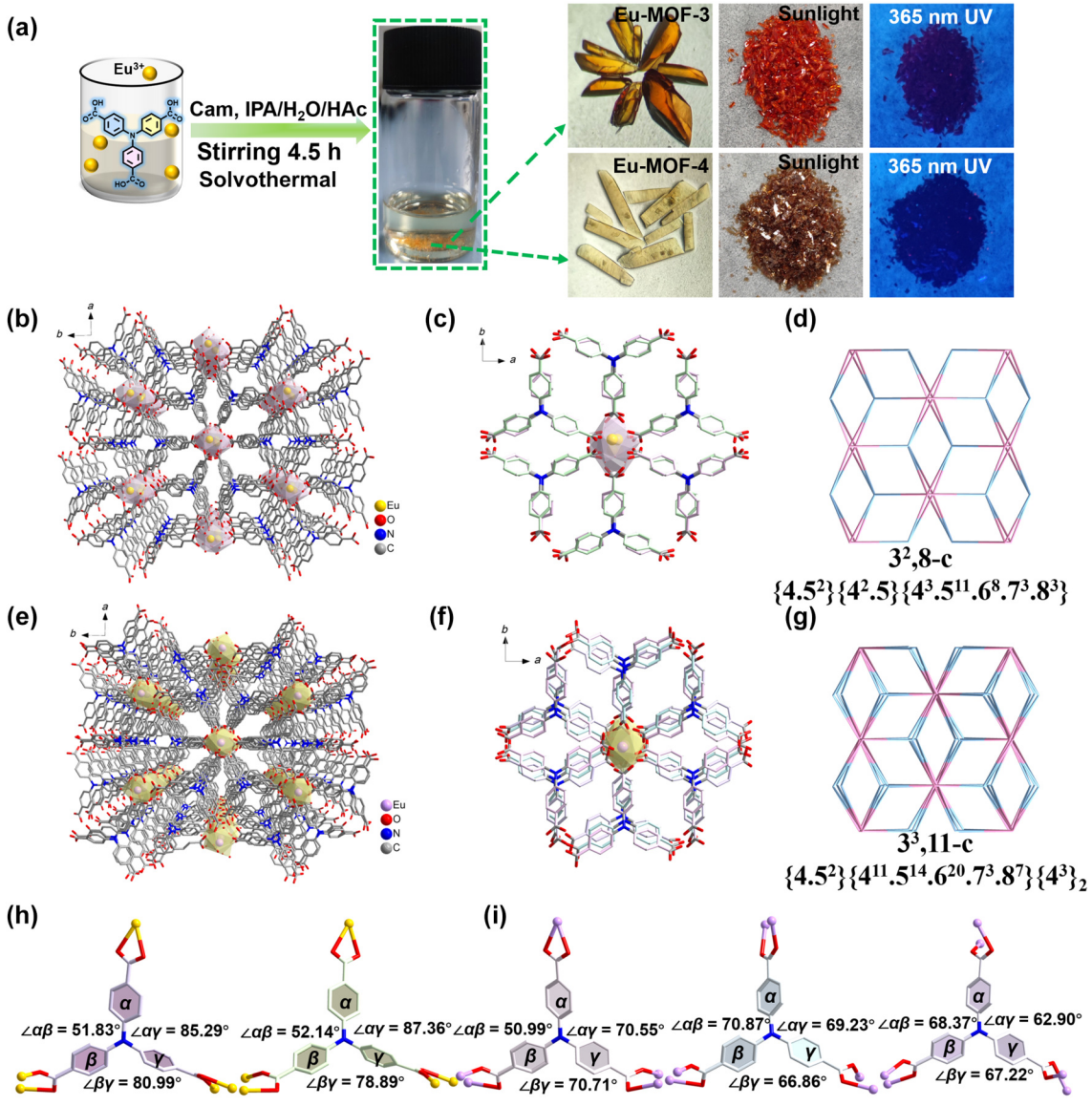

Figure 4 (a) Schematic diagram of the synthesis of Eu-MOF-3/4 from Eu^{3+} and TPA-COOH. ((b) and (e)) Crystal structures of Eu-MOF-3 and Eu-MOF-4. ((c) and (f)) In the *c*-direction, $TPA\text{-}COO^-$ linkers connect the two SBUs of Eu-MOF-3 and Eu-MOF-4. ((d) and (g)) Topological connection modes of Eu-MOF-3 and Eu-MOF-4. ((h) and (i)) Angle between benzene rings and ligand coordination mode on $TPA\text{-}COO^-$.

of Ln-MOFs, we further examined the delayed luminescence spectra and lifetime decay curves of Gd-MOF at various temperatures. The PXRD results of Gd-MOF show that its diffraction peak positions and intensities are highly consistent with the simulated pattern, indicating that the synthesized Gd-MOF is a pure phase and is isostructural with Tb-MOF or Eu-MOF (Fig. S9(h) in the ESM). Experimental findings indicate that the phosphorescence (Phos) intensity of Gd-MOF decreases progressively with rising temperature (Fig. 5(e)), which aligns with the general trend observed in typical long-lasting glow materials. Concurrently, its phosphorescence lifetime shortens from 2419.79 to 164.716 μs (Fig. 5(f)). Time-dependent visible light photographs show that after switching off the 365 nm UV lamp, Gd-MOF continues to emit a long yellow-green afterglow lasting approximately 1.25 s (Fig. 5(h)). This afterglow behavior is primarily attributed to the strong electron donor of the triphenylamine unit, although the framework coordination significantly restricts its molecular conformation. Additionally, the host–guest interaction between the guest molecules in the pores and the main framework contributes to the Gd-MOF's pronounced long afterglow behavior [45–47]. To further investigate the energy transfer process of the antenna effect in Ln-MOFs, the Jablonski energy level diagram was constructed (Fig. 5(g)). First, the energy level of the singlet excited state S_1 was determined to be 30,120 cm^{-1} through the UV–visible absorption spectrum of TPA-COOH (Fig. S13(a) in the ESM). Given that the energy value of the S_1 state of TPA-COOH is obviously lower than the $^6I_{17/2}$ emission level of Gd^{3+} ions (32,500 cm^{-1}), it is evident that TPA-COOH cannot function as an antenna to sensitize Gd^{3+} ions. Therefore, by analyzing the phosphorescence spectrum of Gd-MOF at 77 K and performing Gaussian fitting, the energy level value of its T_1 state was obtained to be 22,026 cm^{-1} (Fig. S13(b) in the ESM). According to Reinhoudt's empirical rule, the energy level difference between the S_1 and T_1 excited states of TPA-COOH ($\Delta E_{S_1 \rightarrow T_1}$) is 8094 cm^{-1}, which is significantly larger than 5000 cm^{-1}, proving that an effective intersystem crossing (ISC) process can occur between the S_1 and T_1

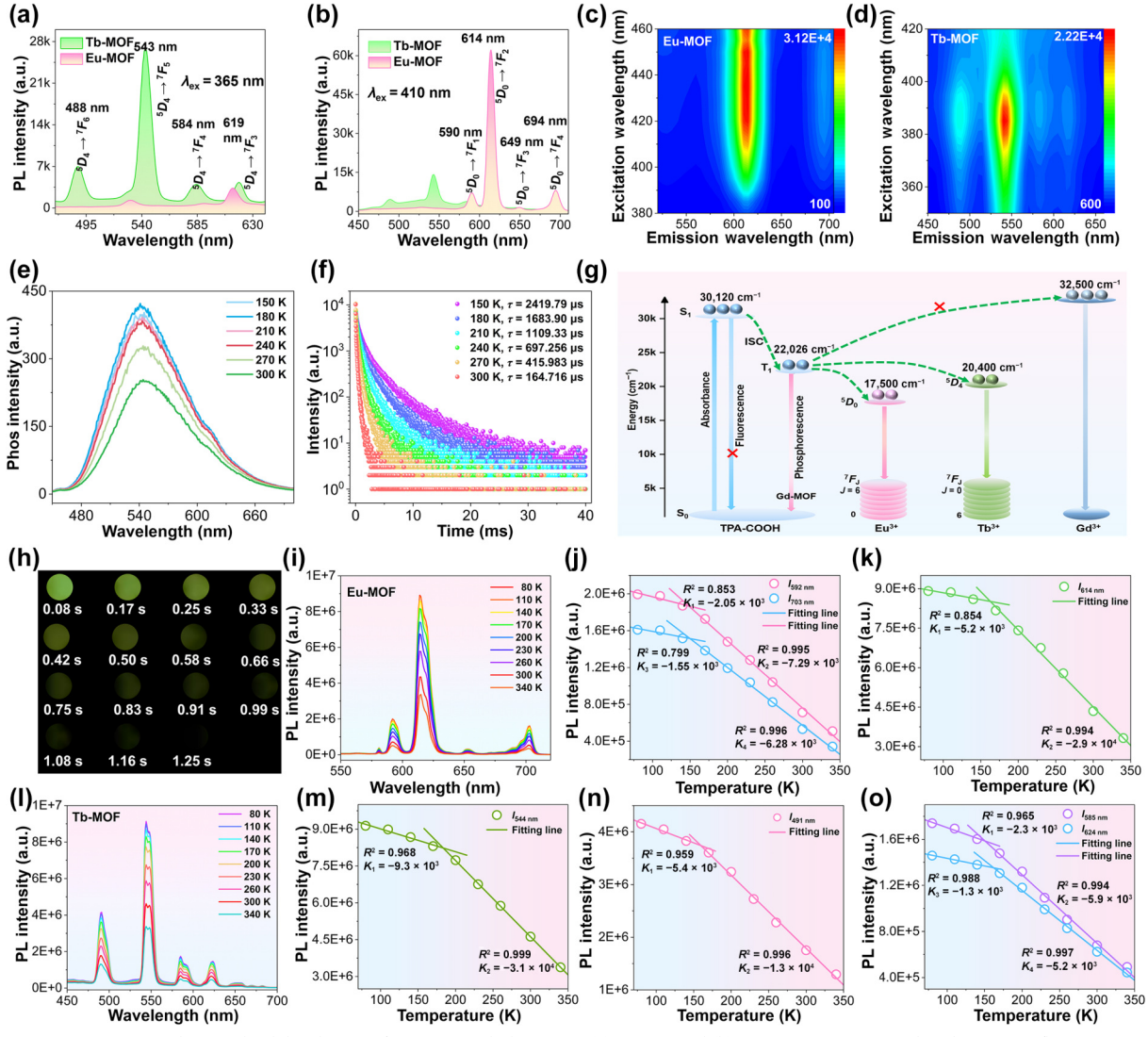

Figure 5 Emission spectra and energy level distribution of Eu-MOF and Tb-MOF at (a) 365 nm and (b) 410 nm excitation wavelength. Contour fluorescence spectra of (c) Eu-MOF and (d) Tb-MOF. (e) Phosphorescence emission spectra of Gd-MOF at different temperatures. (f) Phosphorescence lifetimes of Gd-MOF at different temperatures. (g) Jablonski diagram used to illustrate the ET pathway by which the TPA-COOH ligands act as effective antennas to promote the luminescence of Ln-MOFs. (h) Phosphorescence image of Gd-MOF taken at 77 K. Fluorescence emission spectra of (i) Eu-MOF and (l) Tb-MOF at different temperatures and ((j), (k), and (m)–(o)) curve fitting results.

energy levels of TPA-COOH [36, 37, 48, 49]. According to Latva's empirical rule, the optimal ΔE_1 value for the efficient energy transfer process between TPA-COOH and Eu^{3+} ions is 2000–5000 cm^{-1}, and the ΔE_2 value between the T_1 energy level of TPA-COOH and the $^5D_0$ energy level of Eu^{3+} ions is 4526 cm^{-1}, confirming that TPA-COOH can act as an effective antenna to transfer energy to Eu^{3+} ions. In addition, the T_1 state energy level of TPA-COOH is significantly higher than the $^5D_4$ energy level of Tb^{3+}, proving that the TPA-COOH ligand can undergo energy transfer (ET) process with Tb^{3+} ions, thereby acting as an antenna [50–55]. In addition, we examined the temperature-dependent fluorescence emission spectra of Eu-MOF and Tb-MOF across a temperature range of 80–340 K and performing a linear fit on the relationship between the fluorescence intensity and temperature (Figs. 5(i) and 5(l)). The experimental results indicate that the fluorescence intensity of both Eu-MOF and Tb-MOF gradually diminishes as the temperature rises. Specifically, at lower temperatures, the fluorescence intensity decreases more slowly, whereas at higher temperatures, it shows a more pronounced linear decline (Figs. 5(j), 5(k), and 5(m)–5(o)). In the low-temperature region, the molecular rotor modules within the Eu-MOF and Tb-MOF structures move slowly, and non-radiative transition pathways are significantly suppressed. Therefore, in the low-temperature region, the quenching effect of increasing temperature on the luminescence intensity of Eu-MOF and Tb-MOF is weaker, and the intensity decreases more gradually. In the high-temperature region, the movement of the molecular rotor modules within the Eu-MOF and Tb-MOF structures intensifies dramatically, leading to a significant increase in energy dissipation through non-radiative transition pathways, resulting in a rapid decrease in luminescence intensity with increasing temperature. It is noteworthy that lanthanide luminescent MOFs constructed with planar rotor ligands typically exhibit only a single thermal quenching slope when used as temperature probes [56, 57]. However, the Eu-MOF and Tb-MOF prepared in this study demonstrated distinct temperature response characteristics in the low/high temperature regions. This unique

dual-range response characteristic offers a new method for constructing a ratiometric fluorescence thermometer with high sensitivity over a wide temperature range, particularly in the high-temperature region.

Due to the lanthanide contraction effect, Ln^{3+} ions possess similar coordination structures and physicochemical properties, allowing different Ln^{3+} ions to be uniformly doped in the same framework, this provides an effective strategy for constructing structurally consistent multicolor luminescent MOFs materials [58–63]. A series of $Eu_xTb_{(1-x)}$-MOFs doped with Eu^{3+} and Tb^{3+} ions in different molar ratios were synthesized under solvothermal conditions. Inductively coupled plasma mass spectrometry (ICP-MS) results revealed that the actual ratio of lanthanide ions in the obtained $Eu_xTb_{(1-x)}$-MOFs closely matched the feed ratio (Table S4 in the ESM). In addition, the PXRD spectra of samples with different doping ratios showed no significant changes, indicating that the introduction of Eu^{3+} and Tb^{3+} did not alter the crystal structure of the parent MOFs (Figs. S14(a) and S14(b) in the ESM). We further explored the optical properties of $Eu_xTb_{(1-x)}$-MOFs (x = 0.01–0.90) with different doping ratios. Under 365 nm ultraviolet light excitation, as the Tb^{3+} ion content increases (x decreases from 0.09 to 0.01), the luminescence color of the material transitions continuously from red, orange, and yellow to green (Fig. 6(a)). Emission spectrum analysis reveals that as the Tb^{3+} ion content increases from 91% to 96%, the intensity of the characteristic emission peak at 543 nm (corresponding to the $^5D_4 \rightarrow {}^7F_5$ transition) is notably lower than that of the Eu^{3+} emission peak at 614 nm (Fig. 6(b)). However, when the Tb^{3+} content further rises to between 97% and 99%, the emission intensity at 543 nm is significantly enhanced (Fig. 6(c)). It is worth noting that under 410 nm light excitation, as the Eu^{3+} content increases (x = 0.1–0.9), the luminescent color of the material is predominantly red, shifting

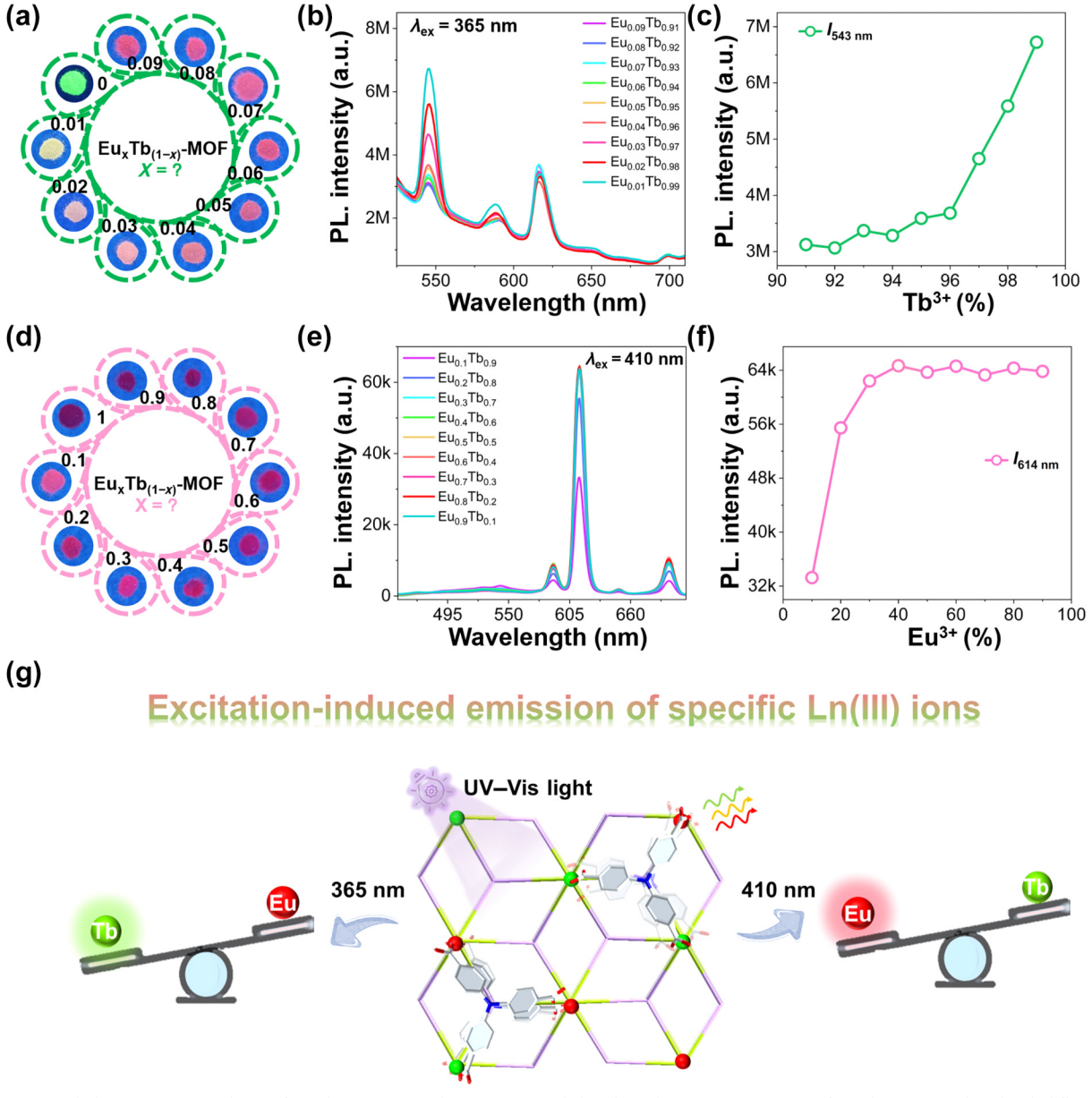

Figure 6 ((a) and (d)) Luminescence photos of $Eu_xTb_{(1-x)}$-MOFs under a 365 nm UV light. ((b) and (e)) Emission spectra of $Eu_xTb_{(1-x)}$-MOFs doped with different ratios of Tb^{3+} and Eu^{3+} ions. ((c) and (f)) Relationship between the emission peak intensity of $Eu_xTb_{(1-x)}$-MOFs and the contents of Tb^{3+} and Eu^{3+} ions, respectively. (g) Schematic diagram of regulating Ln-MOFs luminescence by different excitation wavelengths.

from light red to dark red with an increasing doping ratio (Fig. 6(d)). The emission spectrum indicates that as the Eu^{3+} ion content rises from 10% to 30%, the characteristic emission peak at 614 nm, attributed to the $^5D_0 \rightarrow {}^7F_2$ transition, is significantly enhancesd (Fig. 6(e)). When the Eu^{3+} content reaches 40%, the intensity of the emission peak reaches its maximum; further increasing the Eu^{3+} content does not result in a significant increase in emission intensity, suggesting that the optimal doping ratio of Eu^{3+} is 40%, achieving the best characteristic emission at this composition (Fig. 6(f)). In $Eu_xTb_{(1-x)}$-MOFs, the characteristic emission peak intensity increases rapidly as the Eu^{3+} ions content increases from 10% to 40%. Furthermore, when the Eu^{3+} ions content in the $Eu_xTb_{(1-x)}$-MOFs structure exceeds 40%, the change in its characteristic emission peak intensity is negligible. This phenomenon indicates that even a low content of Eu^{3+} ions in the $Eu_xTb_{(1-x)}$-MOFs structure can still maximize the characteristic emission of Eu^{3+} ions. Conversely, with increasing Tb^{3+} ion content in the $Eu_xTb_{(1-x)}$-MOFs structure (when the content is below 96%), the characteristic emission peak intensity is weak and the change is not significant. When the Tb^{3+} ions content exceeds 96%, the characteristic emission peak intensity of Tb^{3+} ions in the $Eu_xTb_{(1-x)}$-MOFs structure gradually increases. This series of changes indicate that Tb^{3+} ions in the $Eu_xTb_{(1-x)}$-MOFs structure act as an efficient energy transfer medium, enhancing the antenna effect of Eu^{3+} ions and promoting the characteristic emission of Eu^{3+} ions. All in all, by adjusting the excitation wavelength and the doping ratio of lanthanide ions, it is possible to continuously regulate the luminescence color of $Eu_xTb_{(1-x)}$-MOFs and effectively enhance the emission of specific lanthanide ions within it (Fig. 6(g)), providing an experimental basis and material foundation for applications in optical modulation and fluorescence coding.

2.3 Smart anti-counterfeiting applications

Against the backdrop of globalization and the rapid evolution of e-commerce, the pace of commodity circulation has accelerated at an unprecedented rate. However, this has also led to a surge in the problem of counterfeit and substandard products. Counterfeiting not only results in significant economic losses but also poses direct threats to people's lives, health, and the stability of social security and order [64–66]. Consequently, the development of efficient, reliable, and hard-to-replicate anti-counterfeiting technology is of critical importance. Leveraging the distinct luminescence behaviors of Ln-MOFs under 365 and 410 nm excitation, they are applied to information encryption and anti-counterfeiting design. Eu-MOF, $Eu_{0.01}Tb_{0.99}$-MOF, and Tb-MOF were utilized to design a "4 × 4" lattice system for complex data encryption (Fig. 7(a)). In sunlight, all the circular filter papers appear white (coded "00"), with the output information being U (coded "000"). Under 365 nm ultraviolet light, they appear green (Tb-MOF, coded "01") and yellow ($Eu_{0.01}Tb_{0.99}$-MOF, coded "02"), respectively, with the output information being X (coded "121"). Under 410 nm ultraviolet light, only red (Eu-MOF, coded "03") is visible, and the output information is G (coded "333"). In addition, Eu-MOF, $Eu_{0.01}Tb_{0.99}$-MOF, and Tb-MOF were dispersed in polyethylene glycol aqueous solution, and after ultrasonic treatment, a simple ink was formed. This ink was then evenly coated on a circular filter paper and neatly arranged on a black background plate after drying. In sunlight, it appears as a white "8888" pattern, while under 365 nm ultraviolet light, a yellow-green "$3_1^1{}_{11}^1$" pattern is visible to the naked eye, and under 410 nm ultraviolet light, a red "1925" pattern can be observed, demonstrating multimodal optical response and effective visual encryption (Fig. 7(b)). Tb-MOF can also be made into flexible films that can be bent and folded at will without deformation or breakage (Fig. 7(c)). The Fourier transform infrared (FTIR) characteristic absorption peaks of the Tb-MOF thin film are highly consistent with those of Tb-MOF, proving that Tb-MOF remains stable after being fabricated into a thin film (Fig. S15 in the ESM). Furthermore, photonic barcodes, with their small size and unique recognition mechanism, hold great potential for application in material management, information security, anti-counterfeiting, and other fields [67–71]. We achieve anti-counterfeiting and traceability by embedding the traceability code into the photonic barcode. By unlocking the triple password designed based on the "4 × 4" dot matrix system, the cracking instructions are revealed (Fig. 7(d)). Eu-MOF, Tb-MOF, $Eu_{0.01}Tb_{0.99}$-MOF, and $Eu_{0.1}Tb_{0.9}$-MOF were selected to construct the photonic barcode system, with the detailed design strategy provided in the ESM. The barcode consists of two sub-barcodes. Under 365 nm UV light, sub-barcode 1, designed from Tb-MOF and $Eu_{0.01}Tb_{0.99}$-MOF, can be read as "GX192806" using the "scan" function on a mobile phone. However, sub-barcode 2, designed from Eu-MOF and $Eu_{0.1}Tb_{0.9}$-MOF, is read incorrectly under 365 nm UV light, but is read as "QKBCHXZX" under 410 nm UV light (Fig. S16 in the ESM). When combined, the complete traceability code "GX192806QKBCHXZX" is obtained (Fig. 7(e)). This barcode is printed on the packaging of valuable medicines, allowing consumers to enter the code through official channels to query drug information and verify authenticity, thereby achieving dual functions of traceability and anti-counterfeiting.

3 Conclusions

In summary, this work is the first to effortlessly obtain three Ln-MOFs with distinct topological network connections by adjusting the twisting angle of the molecular rotor within the triangular AIEgen structure. Specifically, by altering the type of metal salt, two molecular rotor modules with distinct twisting angles but similar structures, Eu-MOF and Tb-MOF, were successfully synthesized. Both feature 3,8-c connection networks, with topological point symbols of $\{4.5^2\}_2\{4^2.5^{12}.6^4.7^5.8^3.9^2\}$. By further adjusting the reaction conditions and inducing conformational changes in the molecular rotor module of AIEgens, a rare 3^2,8-c connection network (Eu-MOF-1, with topological point symbols of $\{4^2.5\}_2\{4^4.5^9.6^8.7^5.8^2\}$) and a more intricate 3^3,11-c connection network (Eu-MOF-2 and Tb-MOF-1, with topological point symbols of $\{4.5^2\}\{4^{11}.5^{14}.6^{20}.7^3.8^7\}\{4^3\}_2$) were achieved. Additionally, by extending the stirring time, Eu-MOF-3 (topological point symbols of $\{4.5^2\}\{4^2.5\}\{4^3.5^{11}.6^8.7^3.8^3\}$) and Eu-MOF-4 ($\{4.5^2\}\{4^{11}.5^{14}.6^{20}.7^3.8^7\}\{4^3\}_2$) were obtained, with topological connection networks akin to those of Eu-MOF-1 and Eu-MOF-2, respectively. To the best of our knowledge, this study is the first to demonstrate that conformational changes in the molecular rotor module within the AIEgen structure can induce a diverse 3-c-connected network in the Ln-MOFs family. AIEgens with varying twist angles possess different energy levels, allowing them to selectively match the excitation requirements of different lanthanide ions. Consequently, Tb-MOF and Eu-MOF exhibit different optimal excitation wavelengths. In mixed-metal doped $Eu_xTb_{(1-x)}$-MOFs (x = 0.01–0.90), TPA-COOH is highly matched with the energy levels of Tb^{3+} ions at 365 nm excitation wavelength, while it is more easily matched with the energy levels of Eu^{3+} ions at

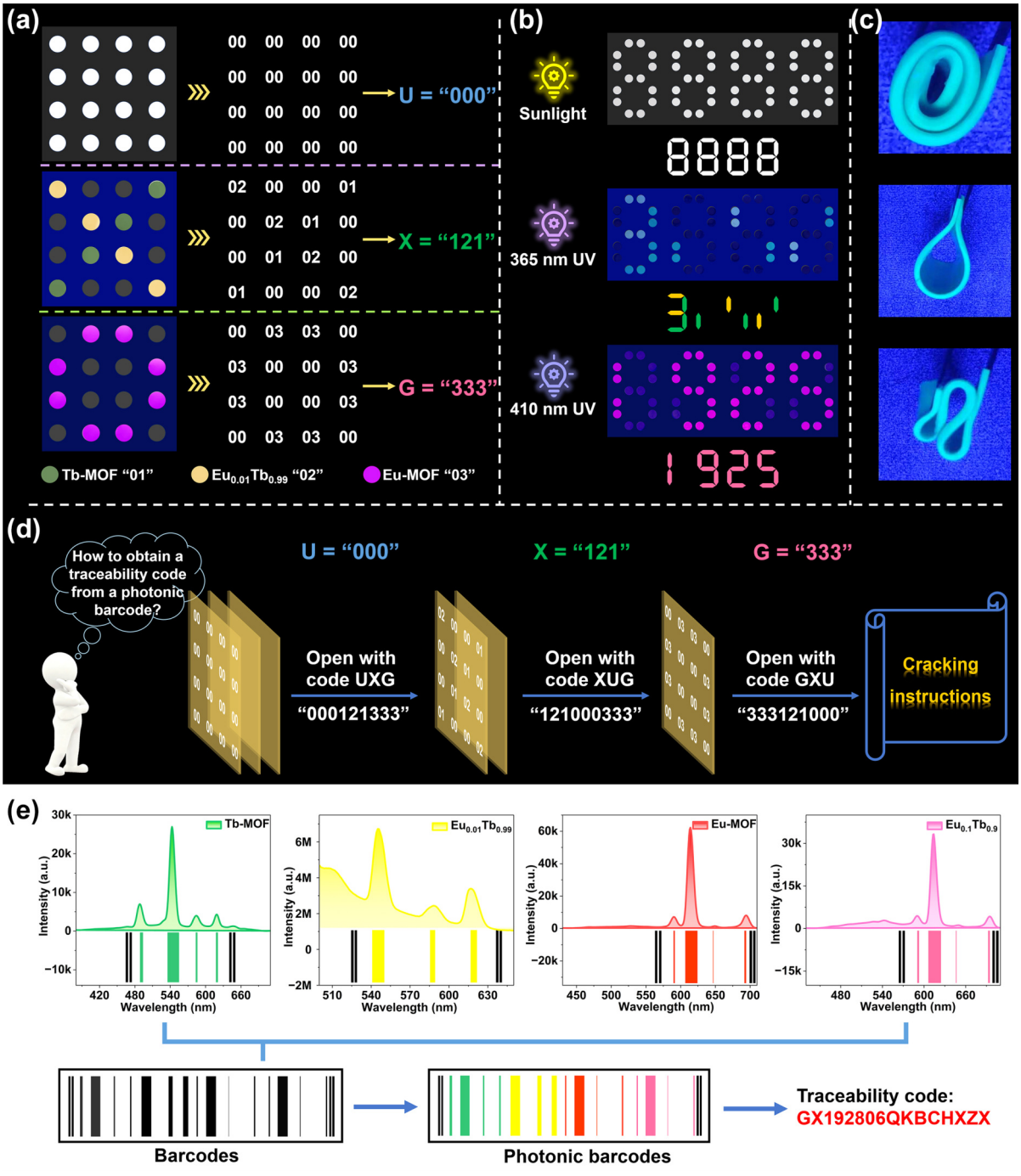

Figure 7 (a) Information encryption and program coding information encryption based on intelligent light response behavior of ultraviolet light of different wavelengths. (b) Changes in the "8888" pattern under 365 and 410 nm UV light. (c) Tb-MOF can be made into flexible thin films. (d) Schematic diagram for obtaining cracking instructions. (e) Schematic diagram of the process of obtaining traceability codes through barcodes designed based on Ln-MOFs.

410 nm excitation, enabling excitation wavelength-dependent selective emission regulation. Eu-/Tb-MOF exhibits linear temperature responses with varying sensitivities in the high/low temperature regions, making it suitable for dual-region ratiometric fluorescence thermometers. In addition, when Tb-MOF is processed into a thin film, its bright green luminescence remains stable after multiple bending, demonstrating excellent processing characteristics and broad device application prospects. This work achieves the controllable construction of Ln-MOFs with diverse topological structures by precisely regulating the twisting angle of the dynamic molecular rotor. This not only broadens the diversity of MOFs structures but also paves the way for constructing multifunctional lanthanide MOFs emitters.

Electronic Supplementary Material: Supplementary material (experimental section, characterization including crystallographic details, FTIR, TG, PXRD, UV–visible absorption spectra, decay curves, SEM, ICP-MS, and QYs of Ln-MOFs) is available in the online version of this article at https://doi.org/10.26599/NR.2026.94908442.

Data availability

All data needed to support the conclusions in the paper are presented in the manuscript and the Electronic Supplementary Material. Additional data related to this paper may be requested from the corresponding author upon request.

Acknowledgements

This work was supported by the National Natural Science Foundation of China (Nos. 22505045 and 22503021), Startup Fund of Guangxi University (Nos. ZX1080030424009 and ZX1080030424008), Natural Science Foundation of Guangxi (No. 2025GXNSFDA069029), and Guangxi University Young and Middle-aged Teachers' Scientific Research Basic Capacity Improvement Project (Nos. 2025KY0055 and 2025KY0054).

Declaration of competing interest

All the contributing authors report no conflict of interests in this work.

Author contribution statement

D.-X. C. and Y.-L. L.: Data curation, project administration, validation, writing manuscript, software, experimental design. R.-Y. L. and W.-W. Q.: Data curation, validation, experimental design. H.-H. Z. and F.-P. L.: Project administration, methodology, resources, supervision. H.-L. W. and Z.-H. Z.: Project administration, funding acquisition, writing – review & editing, visualization, methodology, investigation, formal analysis, funding acquisition. All the authors have approved the final manuscript.

Use of AI statement

None.

References

[1] Yaghi, O. M.; Kalmutzki, M. J.; Diercks, C. S. *Introduction to Reticular Chemistry: Metal-Organic Frameworks and Covalent Organic Frameworks*; Wiley-VCH: Weinheim, 2019.

[2] Furukawa, H.; Cordova, K. E.; O'Keeffe, M.; Yaghi, O. M. The chemistry and applications of metal-organic frameworks. *Science* **2013**, *341*, 1230444.

[3] Kalmutzki, M. J.; Hanikel, N.; Yaghi, O. M. Secondary building units as the turning point in the development of the reticular chemistry of MOFs. *Sci. Adv.* **2018**, *4*, eaat9180.

[4] Zhou, H. C.; Long, J. R.; Yaghi, O. M. Introduction to metal-organic frameworks. *Chem. Rev.* **2012**, *112*, 673–674.

[5] Yuan, S.; Feng, L.; Wang, K. C.; Pang, J. D.; Bosch, M.; Lollar, C.; Sun, Y. J.; Qin, J. S.; Yang, X. Y.; Zhang, P. et al. Stable metal-organic frameworks: Design, synthesis, and applications. *Adv. Mater.* **2018**, *30*, 1704303.

[6] Stock, N.; Biswas, S. Synthesis of metal-organic frameworks (MOFs): Routes to various MOF topologies, morphologies, and composites. *Chem. Rev.* **2012**, *112*, 933–969.

[7] Wang, Z. Q.; Cohen, S. M. Postsynthetic modification of metal-organic frameworks. *Chem. Soc. Rev.* **2009**, *38*, 1315–1329.

[8] Teffu, D. M.; Makgopa, K.; Somo, T. R.; Ratsoma, M. S.; Honey, S.; Makhado, E.; Modibane, K. D. Metal and covalent organic frameworks (MOFs and COFs): A comprehensive overview of their synthesis, characterization and enhanced supercapacitor performance. *Coord. Chem. Rev.* **2025**, *540*, 216798.

[9] Liang, Z. Z.; Wang, H. Y.; Zheng, H. Q.; Zhang, W.; Cao, R. Porphyrin-based frameworks for oxygen electrocatalysis and catalytic reduction of carbon dioxide. *Chem. Soc. Rev.* **2021**, *50*, 2540–2581.

[10] Lu, W. G.; Wei, Z. W.; Gu, Z. Y.; Liu, T. F.; Park, J.; Park, J.; Tian, J.; Zhang, M. W.; Zhang, Q.; Gentle III, T. et al. Tuning the structure and function of metal-organic frameworks via linker design. *Chem. Soc. Rev.* **2014**, *43*, 5561–5593.

[11] Mei, J.; Leung, N. L. C.; Kwok, R. T. K.; Lam, J. W. Y.; Tang, B. Z. Aggregation-induced emission: Together we shine, united we soar! *Chem. Rev.* **2015**, *115*, 11718–11940.

[12] Luo, J. D.; Xie, Z. L.; Lam, J. W. Y.; Cheng, L.; Chen, H. Y.; Qiu, C. F.; Kwok, H. S.; Zhan, X. W.; Liu, Y. Q.; Zhu, D. B. et al. Aggregation-induced emission of 1-methyl-1,2,3,4,5-pentaphenylsilole. *Chem. Commun.* **2001**, *18*, 1740–1741.

[13] Xu, S. D.; Duan, Y. K.; Liu, B. Precise molecular design for high-performance luminogens with aggregation-induced emission. *Adv. Mater.* **2020**, *32*, 1903530.

[14] Dong, J. Q.; Wee, V.; Zhao, D. Stimuli-responsive metal-organic frameworks enabled by intrinsic molecular motion. *Nat. Mater.* **2022**, *21*, 1334–1340.

[15] Dong, J. Q.; Wee, V.; Peh, S. B.; Zhao, D. Molecular-rotor-driven advanced porous materials. *Angew. Chem., Int. Ed.* **2021**, *60*, 16279–16292.

[16] Li, Y. L.; Wang, H. L.; Ai, J. F.; Zhang, G. H.; Zou, H. H.; Liang, F. P.; Zhu, Z. H. Respiration drives dynamic metal-organic framework for smart photoresponse to volatile toxic vapors and their photodynamic sterilization. *Adv. Sci.* **2025**, *12*, 2501824.

[17] Zhu, Z. H.; Ni, Z. Q.; Zou, H. H.; Feng, G. X.; Tang, B. Z. Smart metal-organic frameworks with reversible luminescence/magnetic switch behavior for HCl vapor detection. *Adv. Funct. Mater.* **2021**, *31*, 2106925.

[18] Zhu, Z. H.; Bi, C. J.; Zou, H. H.; Feng, G. X.; Xu, S. P.; Tang, B. Z. Smart tetraphenylethene-based luminescent metal-organic frameworks with amide-assisted thermofluorochromics and piezofluorochromics. *Adv. Sci.* **2022**, *9*, 2200850.

[19] Lang, F. F.; Pang, J. D.; Bu, X. H. Stimuli-responsive coordination polymers toward next-generation smart materials and devices. *eScience* **2024**, *4*, 100231.

[20] Zhang, Q.; Su, J.; Feng, D. W.; Wei, Z. W.; Zou, X. D.; Zhou, H. C. Piezofluorochromic metal-organic framework: A microscissor lift. *J. Am. Chem. Soc.* **2015**, *137*, 10064–10067.

[21] Liu, C. Y.; Chen, X. R.; Chen, H. X.; Niu, Z.; Hirao, H.; Braunstein, P.; Lang, J. P. Ultrafast luminescent light-up guest detection based on the lock of the host molecular vibration. *J. Am. Chem. Soc.* **2020**, *142*, 6690–6697.

[22] Shang, W. L.; Zhu, X. F.; Liang, T. L.; Du, C.; Hu, L. Y.; Li, T. S.; Liu, M. H. Chiral reticular self-assembly of achiral AIEgen into optically pure metal-organic frameworks (MOFs) with dual mechano-switchable circularly polarized luminescence. *Angew. Chem., Int. Ed.* **2020**, *59*, 12811–12816.

[23] Liu, Y. Y.; Zhang, X.; Li, K.; Peng, Q. C.; Qin, Y. J.; Hou, H. W.; Zang, S. Q.; Tang, B. Z. Restriction of intramolecular vibration in aggregation-induced emission luminogens: Applications in multifunctional luminescent metal–organic frameworks. *Angew. Chem., Int. Ed.* **2021**, *60*, 22417–22423.

[24] Chen, Y. W.; Xie, H. M.; Wang, X. J.; Sha, F. R.; Kirlikovali, K. O.; Wang, X. L.; Ye, Z. M.; Tang, X. H.; Zhang, C. H.; Peterson, G. W. et al. Leveraging ligand desymmetrization to enrich structural diversity of zirconium metal-organic frameworks for toxic chemical adsorption. *Angew. Chem., Int. Ed.* **2025**, *64*, e202417664.

[25] Kong, X. J.; Xie, H. M.; He, T.; Liu, J. Y.; Wang, X. L.; Cheng, Z. H.; Kirlikovali, K. O.; Ye, Z. M.; Farha, O. K. Reticular structural diversification of zirconium metal-organic frameworks through angular ligand configuration control. *J. Am. Chem. Soc.* **2025**, *147*, 18963–18971.

[26] Hu, Z. C.; Lustig, W. P.; Zhang, J. M.; Zheng, C.; Wang, H.; Teat, S. J.; Gong, Q. H.; Rudd, N. D.; Li, J. Effective detection of mycotoxins by a highly luminescent metal-organic framework. *J. Am. Chem. Soc.* **2015**, *137*, 16209–16215.

[27] Guo, X. L.; Zhu, N. S.; Wang, S. P.; Li, G. H.; Bai, F. Q.; Li, Y.; Han, Y. H.; Zou, B.; Chen, X. B.; Shi, Z. et al. Stimuli-responsive luminescent properties of tetraphenylethene-based strontium and cobalt metal-organic frameworks. *Angew. Chem., Int. Ed.* **2020**, *59*, 19716–19721.

[28] Yin, H. Q.; Wang, X. Y.; Yin, X. B. Rotation restricted emission and antenna effect in single metal-organic frameworks. *J. Am. Chem. Soc.* **2019**, *141*, 15166–15173.

[29] Li, Z. J.; Zhang, J. P.; Wu, Z. Y.; Lei, H.; Zhao, Y. F.; Qi, W. Q.; Gao, X.; Jiang, F. L.; Liu, Y. S.; Chen, L. et al. A sensitive ratiometric thermometer constructed by AIEgen-based mixed lanthanide MOF for intracellular temperature mapping. *Adv. Sci.* **2025**, *12*, e10147.

[30] Li, Y. L.; Wang, H. L.; Xiao, Z. X.; Ai, J. F.; Liang, F. P.; Zhu, Z. H.; Zou, H. H. Dynamic rare-earth metal-organic frameworks based on molecular rotor linkers with efficient emissions and ultrasensitive optical sensing performance. *ACS Appl. Mater. Interfaces* **2024**, *16*, 62301–62313.

[31] Wu, P. Y.; Wang, J.; He, C.; Zhang, X. L.; Wang, Y. T.; Liu, T.; Duan, C. Y. Luminescent metal-organic frameworks for selectively sensing nitric oxide in an aqueous solution and in living cells. *Adv. Funct. Mater.* **2012**, *22*, 1698–1703.

[32] Yao, Z. Q.; Wang, K.; Liu, R.; Yuan, Y. J.; Pang, J. J.; Li, Q. W.; Shao, T. Y.; Li, Z. G.; Feng, R.; Zou, B. et al. Dynamic full-color tuning of organic chromophore in a multi-stimuli-responsive 2D flexible MOF. *Angew. Chem., Int. Ed.* **2022**, *61*, e202202073.

[33] Wang, H. L.; Li, Y. L.; Zou, H. H.; Liang, F. P.; Zhu, Z. H. Smart lanthanide metal-organic frameworks with multicolor luminescence switching induced by the dynamic adaptive antenna effect of molecular rotors. *Adv. Mater.* **2025**, *37*, 2502742.

[34] Li, Z. J.; Jiang, F. L.; Yu, M. X.; Li, S. C.; Chen, L.; Hong, M. C. Achieving gas pressure-dependent luminescence from an AIEgen-based metal-organic framework. *Nat. Commun.* **2022**, *13*, 2142.

[35] Pang, J. J.; Yao, Z. Q.; Zhang, K.; Li, Q. W.; Fu, Z. X.; Zheng, R.; Li, W.; Xu, J.; Bu, X. H. Real-time *in situ* volatile organic compound sensing by a dual-emissive polynuclear Ln-MOF with pronounced Ln^{III} luminescence response. *Angew. Chem., Int. Ed.* **2023**, *62*, e202217456.

[36] Tang, M. J.; Zhu, Z. H.; Wang, H. L.; Liang, F. P.; Zou, H. H. Mitochondria-targeted and magnetic resonance imaging of water-stable trilobate-shaped nonanuclear lanthanide clusters. *Chin. Chem. Lett.*, in press, https://doi.org/10.1016/j.cclet.2025.112126.

[37] Yang, F.; Zhang, G. H.; Wang, H. L.; Qin, W. W.; Zhu, Z. H.; Liang, F. P.; Zou, H. H. Ultrasonic cutting strategy yields lanthanide organic nanochains with bright emission: Thermally enhanced luminescence and bio-optical imaging. *Chin. J. Struct. Chem.* **2026**, *45*, 100761.

[38] Allendorf, M. D.; Bauer, C. A.; Bhakta, R. K.; Houk, R. J. T. Luminescent metal-organic frameworks. *Chem. Soc. Rev.* **2009**, *38*, 1330–1352.

[39] Hu, Z. C.; Deibert, B. J.; Li, J. Luminescent metal-organic frameworks for chemical sensing and explosive detection. *Chem. Soc. Rev.* **2014**, *43*, 5815–5840.

[40] Zhang, G. H.; Wang, H. L.; Cheng, L.; Li, Y. L.; Zhu, Z. H.; Zou, H. H. Hourglass-shaped europium cluster-based secondary building unit in metal-organic framework for photocatalytic wastewater purification and sterilization via enhanced reactive oxygen species production. *J. Colloid Interface Sci.* **2025**, *679*, 578–587.

[41] Zhao, W. J.; He, Z. K.; Tang, B. Z. Room-temperature phosphorescence from organic aggregates. *Nat. Rev. Mater.* **2020**, *5*, 869–885.

[42] Su, Y.; Phua, S. Z. F.; Li, Y. B.; Zhou, X. J.; Jana, D.; Liu, G. F.; Lim, W. Q.; Ong, W. K.; Yang, C. L.; Zhao, Y. L. Ultralong room temperature phosphorescence from amorphous organic materials toward confidential information encryption and decryption. *Sci. Adv.* **2018**, *4*, eaas9732.

[43] Huang, G. Q.; Xia, R. Q.; Chen, X.; Yang, H.; Huang, Y. L.; Wu, K.; Zheng, J.; Lu, W. G.; Li, D. Enabling thermally stimulated delayed phosphorescence in Cu(I) cyclic trinuclear complexes with near-unity quantum yield. *J. Am. Chem. Soc.* **2025**, *147*, 6415–6426.

[44] Ma, F. L.; Wu, B.; Zhang, S. W.; Jiang, J. H.; Shi, J. H.; Ding, Z. Y.; Zhang, Y.; Tan, H. Z.; Alam, P.; Lam, J. W. Y. et al. Lone pairs-mediated multiple through-space interactions for efficient room-temperature phosphorescence. *J. Am. Chem. Soc.* **2025**, *147*, 10803–10814.

[45] Xu, Z. R.; Huang, Y. F.; Sun, S. Y.; Ma, L. W.; Ding, B. B.; Tian, H.; Ma, X. Full-color programmable high temperature afterglow polymers based on single-molecule emitters. *Nat. Commun.* **2025**, *16*, 9668.

[46] Xiong, S. D.; Xiong, Y.; Wang, D. L.; Pan, Y. W.; Chen, K. Y.; Zhao, Z.; Wang, D.; Tang, B. Z. Achieving tunable organic afterglow and UV-irradiation-responsive ultralong room-temperature phosphorescence from pyridine-substituted triphenylamine derivatives. *Adv. Mater.* **2023**, *35*, 2301874.

[47] Su, X. L.; Kong, X. Y.; Sun, K. S.; Liu, Q.; Pei, Y. T.; Hu, D. H.; Xu, M.; Feng, W.; Li, F. Y. Enhanced blue afterglow through molecular fusion for bio-applications. *Angew. Chem., Int. Ed.* **2022**, *61*, e202201630.

[48] Steemers, F. J.; Verboom, W.; Reinhoudt, D. N.; van der Tol, E. B.; Verhoeven, J. W. New sensitizer-modified calix[4]arenes enabling near-UV excitation of complexed luminescent lanthanide ions. *J. Am. Chem. Soc.* **1995**, *117*, 9408–9414.

[49] Li, R. Y.; Tang, M. J.; Li, Y. L.; Yang, F.; Zou, H. H.; Wang, H. L.; Zhu, Z. H. Improving the conjugation of organic ligands enhances the antenna effect and promotes the luminescence and optical imaging of chiral mononuclear Eu(III) complexes. *Chem. Sci.*, in press, https://doi.org/10.1039/D5SC09594H.

[50] Tian, D. S.; Liu, Y. Y.; Kang, Y.; Zhao, Y.; Li, P. C.; Xu, C.; Wang, L. A simple yet efficient hydrophilic phenanthroline-based ligand for selective Am(III) separation under high acidity. *ACS Cent. Sci.* **2023**, *9*, 1642–1649.

[51] Hu, Y. S.; Fang, R. Y.; Liu, Y. H.; Fu, M. H.; Wang, S. H.; Yuan, J. W.; Yang, Q.; Peng, Q. C.; Wang, Z. Y.; Li, X. Q. et al. Temperature-inert terbium cluster scintillator. *Aggregate* **2025**, *6*, e70140.

[52] Li, Y. L.; Wang, H. L.; Zhu, Z. H.; Wang, Y. F.; Liang, F. P.; Zou, H. H. Aggregation induced emission dynamic chiral europium(III) complexes with excellent circularly polarized luminescence and smart sensors. *Nat. Commun.* **2024**, *15*, 2896.

[53] Wang, H. L.; Yu, B.; Liang, F. P.; Zou, H. H. Aggregation-enhanced antenna effects of dynamic chiral Eu(III) complexes significantly enhance imaging of living cells and zebrafish. *Chin. Chem. Lett.*, in press, https://doi.org/10.1016/j.cclet.2025.111346.

[54] Tang, M. J.; Zhu, Z. H.; Li, Y. L.; Qin, W. W.; Liang, F. P.; Wang, H. L.; Zou, H. H. Specific smart sensing of electron-rich antibiotics or histidine improves the antenna effect, luminescence, and photodynamic sterilization capabilities of lanthanide polyoxometalates. *J. Colloid Interface Sci.* **2025**, *680*, 235–246.

[55] Yu, B.; Zhu, Z. H.; Qin, W. W.; Wang, H. L.; Li, Y. L.; Liang, F. P.; Zou, H. H. Enhancement of luminescence, multiple-sensing, and differentiated live-cell-imaging properties of high-nuclear lanthanide nanoclusters via the Zn(II)-chelate-controlled dual antenna effect. *ACS Mater. Lett.* **2024**, *6*, 3312–3326.

[56] Li, T. T.; Liu, J. Z.; Zheng, S. J.; Jiang, F.; Liu, J. Y.; Dong, W. N.; Zhang, Y.; Zheng, S. P.; Li, Y. N.; Wu, Z. N. et al. Heteronuclear lanthanide titanium-oxygen cluster luminescence thermometer with adjustable operating range and sensitivity. *Rare Met.* **2025**, *44*, 2438–2449.

[57] Deng, X.; Li, R.; Zhou, L. P.; Duan, X. F.; Cheng, X. Y.; Hu, S. J.; Sun, Q. F. Tunable luminescence and ratiometric temperature sensing

by hierarchical self-assembly of lanthanide-organic cage. *Nano Res.* **2025**, *18*, 94907327.

[58] Wang, M. M.; Han, Z. S.; Wang, K. Y.; Zhao, B.; Sun, T. K.; Wu, Y. W.; Cheng, P.; Shi, W. Confinement of p-Xylene in the pores of a bilanthanide metal-organic framework for highly selective recognition. *Angew. Chem., Int. Ed.* **2024**, *63*, e202318722.

[59] Han, Z. S.; Wang, K. Y.; Zhou, H. C.; Cheng, P.; Shi, W. Preparation and quantitative analysis of multicenter luminescence materials for sensing function. *Nat. Protoc.* **2023**, *18*, 1621–1640.

[60] Han, Z. S.; Wang, K. Y.; Chen, Y. L.; Li, J. N.; Teat, S. J.; Yang, S. H.; Shi, W.; Cheng, P. A multicenter metal-organic framework for quantitative detection of multicomponent organic mixtures. *CCS Chem.* **2022**, *4*, 3238–3245.

[61] Gálico, D. A.; Murugesu, M. Controlling the energy-transfer processes in a nanosized molecular upconverter to tap into luminescence thermometry application. *Angew. Chem., Int. Ed.* **2022**, *61*, e202204839.

[62] Calado, C. M. S.; Gálico, D. A.; Murugesu, M. Composition control in molecular cluster-aggregates: A toolbox for optical output tunability via energy transfer pathways. *ACS Appl. Mater. Interfaces* **2023**, *15*, 44137–44146.

[63] Gálico, D. A.; Ovens, J. S.; Sigoli, F. A.; Murugesu, M. Room-temperature upconversion in a nanosized $\{Ln_{15}\}$ molecular cluster-aggregate. *ACS Nano* **2021**, *15*, 5580–5585.

[64] Jiang, Y. H.; Fan, Y. F.; Chen, L. M.; Lin, H. Y.; Gao, J. H. Super-multiplexed imaging and coding in the range of radio frequency. *Nat. Commun.* **2025**, *16*, 2567.

[65] Yang, S.; Xu, Y. Y.; Lin, R.; Feng, X. W.; Wang, K.; Wang, Z. T.; Cui, K.; Chen, S. W.; Wang, Z. F.; Wang, X. et al. Conformation-driven responsive 1D and 2D lanthanide-metal-organic framework heterostructures for high-security photonic barcodes. *Small* **2024**, *20*, 2402890.

[66] Jia, S. Z.; Yang, B. B.; Xie, Y. J.; Tao, T. T.; Du, J.; Yu, L. Y.; Zhang, Y.; Zhang, J. Y.; Tang, W. W.; Gong, J. B. Dual-direction circularly polarized luminescence materials with on-demand handedness and superior flexibility. *Adv. Funct. Mater.* **2024**, *34*, 2410206.

[67] Shikha, S.; Salafi, T.; Cheng, J. T.; Zhang, Y. Versatile design and synthesis of nano-barcodes. *Chem. Soc. Rev.* **2017**, *46*, 7054–7093.

[68] Feng, X. W.; Lin, R.; Yang, S.; Xu, Y. Y.; Zhang, T. J.; Chen, S. W.; Ji, Y. K.; Wang, Z. F.; Chen, S. W.; Zhu, C. F. et al. Spatially resolved organic whispering-gallery-mode hetero-microrings for high-security photonic barcodes. *Angew. Chem., Int. Ed.* **2023**, *62*, e202310263.

[69] Yao, Y. N.; Gao, Z. H.; Lv, Y. C.; Lin, X. Q.; Liu, Y. Y.; Du, Y. X.; Hu, F. Q.; Zhao, Y. S. Heteroepitaxial growth of multiblock Ln-MOF microrods for photonic barcodes. *Angew. Chem., Int. Ed.* **2019**, *58*, 13803–13807.

[70] Pei, K.; Wu, J.; Zhao, M.; Feng, X.; Li, Y.; Ma, Y.; Li, H. Q.; Zhai, T. Y. Polarized emission of lanthanide metal-organic framework (Ln-MOF) crystals for high-capacity photonic barcodes. *Adv. Opt. Mater.* **2022**, *10*, 2102143.

[71] Qin, W. W.; Wang, H. L.; Li, Y. L.; Liang, F. P.; Zhu, Z. H.; Zou, H. H. Regulating energy transfer pathways to construct multicolor luminescent lanthanide metal-organic frameworks and their multiorder anticounterfeiting barcodes and antibiotic sensing. *ACS Mater. Lett.* **2024**, *6*, 4911–4921.